Author/s:
Besford, QA;Weiss, ACG;Schubert, J;Ryan, TM;Maitz, MF;Tomanin, PP;Savioli, M;Werner, C;Fery, A;Caruso, F;Cavalieri, F

Title:
Protein Component of Oyster Glycogen Nanoparticles: An Anchor Point for Functionalization

Date:
2020-09-02

Citation:
Besford, Q. A., Weiss, A. C. G., Schubert, J., Ryan, T. M., Maitz, M. F., Tomanin, P. P., Savioli, M., Werner, C., Fery, A., Caruso, F. & Cavalieri, F. (2020). Protein Component of Oyster Glycogen Nanoparticles: An Anchor Point for Functionalization. ACS Applied Materials and Interfaces, 12 (35), pp.38976-38988. https://doi.org/10.1021/acsami.0c10699.

Persistent Link:
https://hdl.handle.net/11343/241961

The Protein Component of Oyster Glycogen Nanoparticles: An Anchor Point for Functionalization

Quinn A. Besford, [†,*] *Alessia C. G. Weiss,* [†] *Jonas Schubert,* [†] *Timothy M. Ryan,* [‡] *Manfred F. Maitz,* [†] *Pietro Pacchin Tomanin,* [§] *Marco Savioli,* [§] *Carsten Werner,* [†] *Andreas Fery,* [†] *Frank Caruso,* [§,*] *Francesca Cavalieri*[*,#,⊥]

[†]Leibniz Institute for Polymer Research, Hohe Straße 6, 01069 Dresden, Germany

[‡]The Australian Synchrotron, Clayton, Victoria 3168, Australia

[§]ARC Centre of Excellence in Convergent Bio-Nano Science and Technology, and the Department of Chemical Engineering, The University of Melbourne, Parkville, Victoria 3010, Australia

[#] School of Science, RMIT University, Melbourne, Victoria 3000, Australia

[⊥] Dipartimento di Scienze e Tecnologie Chimiche, Università di Roma "Tor Vergata", Via Della Ricerca Scientifica 1, 00133, Rome, Italy

*E-mail: besford@ipfdd.de, fcaruso@unimelb.edu.au, francesca.cavalieri@rmit.edu.au

KEYWORDS: glycogen, nanoparticles, poly(*N*-isopropylacrylamide), biopolymers, temperature responsiveness

ABSTRACT

Bio-sourced nanoparticles have a range of desirable properties for therapeutic applications, including biodegradability and low immunogenicity. Glycogen, a natural polysaccharide nanoparticle, has garnered much interest as a component of advanced therapeutic materials. However, functionalizing glycogen for use as a therapeutic material typically involves synthetic approaches that can negatively affect the intrinsic physiological properties of glycogen. Herein, the protein component of glycogen is examined as an anchor point for the photopolymerization of functional poly(*N*-isopropylacrylamide) (PNIPAM) polymers. Oyster glycogen (OG) nanoparticles partially degrade to smaller spherical particles in the presence of protease enzymes, reflecting a population of surface-bound proteins on the polysaccharide. The grafting of PNIPAM to the native protein component of OG produces OG-PNIPAM nanoparticles of ~45 nm in diameter and 6.2 MDa in molecular weight. PNIPAM endows the nanoparticles with temperature-responsive aggregation properties that are controllable, reversible, and which can be removed by the biodegradation of the protein. The OG-PNIPAM nanoparticles retain the native biodegradability of glycogen. Whole blood incubation assays revealed that the OG-PNIPAM nanoparticles have a low cell association and inflammatory response similar to that of OG. The reported strategy provides functionalized glycogen nanomaterials that retain their inherent biodegradability and low immune cell association.

INTRODUCTION

The complex biological environment presents numerous obstacles to the development of new functional nanoparticles for the therapeutic treatment and diagnosis of disease. The success of nanoparticles in achieving their therapeutic potential, particularly in targeted gene and drug delivery, hinges on the ability of the nanoparticles to (1) negotiate the immune system,[1-2] (2) degrade or be excreted in such a way and on a timescale so as to not induce secondary long-term effects,[3-5] and (3) preserve their functionality within the complex biological milieu. The physiological response to nanoparticles varies considerably depending on the type of material (surface chemistry,[6] charge[7]) and physical properties (size, shape and mechanical properties[8-9]) of the nanoparticles. Additional functionality, including temperature, pH, light, and solute responsiveness, is often needed and can be endowed through post-modification of the nanoparticles. The added functionality can enable the nanoparticles to, for example, switch hydrophobicity, charge, or morphology, thus overcoming the "fixed surface dilemma", where nanoparticles with non-tunable surface properties present difficulties in overcoming obstacles imposed by the heterogenous extracellular and intracellular barriers in vivo.[10]

Although synthetic nanoparticle systems offer advantageous platforms to potentially achieve the desired therapeutic outcomes, their application can be limited because of non-degradability of the nanoparticle system or long-term side effects induced by the nanoparticle system,[11] especially with regard to unknown biotransformation processes.[12-14] This has stimulated interest in using natural biopolymers as alternatives to first-generation synthetic nanomaterials—in other words, using materials taken from biology and reintegrating them with a therapeutic purpose. The use of biopolymers is ideal largely because of their numerous advantages such as non-cytotoxicity, biodegradability, high aqueous solubility, large-scale production capability, and their ability to

self-organize into complex structures.[15-16] Examples of natural biopolymer nanoparticle systems include intracellularly assembled structures, such as magnetosomes,[17] ferritin,[18] and glycogen,[19] and extracellularly assembled structures such as lipoproteins[20] and viruses.[21] These biologically synthesized nanoparticles are highly diverse and possess a relatively uniform structure, low toxicity, and some ability to evade the immune system.[22-23] Of these natural nanoparticle systems, glycogen, a highly branched polysaccharide nanoparticle, is one of the most readily available and versatile nanoparticles. Recently, glycogen has gained attention as an advanced material for various therapeutic-based applications,[24-25] including for use as cancer targeting[26] and penetrating nanoparticles,[27] as in vivo contrast agents[28] and immunomodulators,[29] and as a component in biodegradable hydrogels,[30] films,[31] and fibers.[32-33]

The intracellular synthesis of glycogen is highly regulated by various enzymatic cascades, where the biochemical pathways are uniquely adapted to the metabolic demands of each cell type, resulting in different particle structures between sources.[19, 34-37] The particle size spans from approximately 20 to 150 nm, and the particle structure consists of α-1,4 glycosidic chains of D-glucose with α-1,6 branching and a small amount of associated and bound proteins.[38-39] From a material science perspective, glycogen can be obtained commercially from various sources[36] and modified both enzymatically and synthetically.[24] Several synthetic methods to endow glycogen with functionality include periodate oxidation with subsequent reductive amination,[27] *N*,*N*′-carbonyl diimidazole activation of the hydroxyl groups followed by amide formation with primary amine-containing molecules,[30] carbodiimide-catalyzed esterification of the hydroxyl groups with carboxylate-containing molecules in the presence of a base,[31] and etherification of the hydroxyl groups with an alkylating agent in the presence of a base.[26] These synthetic methods exploit the modification of the glycosidic component of glycogen, which can influence the biodegradation[27]

and immunostimulation of the particles. For example, glycogen modified with octenyl succinate moieties and complexed with ovalbumin induced a transient inflammatory response at the injection site in mice, which is thought to occur partly because of the delivery of the antigen to the dendritic cells.[29, 40] Furthermore, the macrophage-stimulating activity of different glycogens has been suggested to correlate to the molecular weight of the particles,[41] which is therefore important to consider when modifying the particles with another polymer. One aspect that remains largely unexplored, to our knowledge, is the modification of the protein component of glycogen. Such an anchor point has the potential to expand the possibilities for modifying glycogen with switchable functionality while providing a facile alternative to complex synthetic additions.

Herein, we show how glycogen's natural protein component can be exploited as an anchor point for the photopolymerization of temperature-responsive polymers, which preserves the biodegradability and immune cell association of glycogen. We report a structural study of the protein component of natural glycogen nanoparticles and show how it acts to conserve particle size. After removal of the protein component with protease, glycogen particles isolated from oysters became significantly smaller and more spherical-like in shape, as determined from size exclusion chromatography (SEC)–small-angle X-ray scattering (SAXS) experiments. These changes indicated the presence of a surface-associated population of proteins on the oyster glycogen (OG) nanoparticles, which were subsequently exploited as anchor points for the free radical photopolymerization of *N*-isopropylacrylamide (NIPAM) from the free thiol groups in the cysteine moieties. The resulting product contained PNIPAM chains tethered to the surface of the nanoparticles, endowing the glycogen-PNIPAM nanoparticles with temperature-responsive aggregation properties. The temperature-induced aggregation of these glyco-clusters was finely controlled and reversible, of which the extent was dependent on the quantity of PNIPAM on the

particles, which could be removed through action of protease digestion enzymes. Functionalizing the protein component of the glycogen nanoparticles with PNIPAM did not significantly influence the inflammation response and association of the nanoparticles with human immune cells in whole blood. The glycogen-PNIPAM particles retained both a biodegradability toward α-amylase degradation and a low association with human immune cells, similar to the glycogen nanoparticles. The present findings highlight a strategy to functionalize natural glycogen nanoparticles with tunable surface chemistry that does not compromise the biodegradability or immune system association of the nanoparticle system.

EXPERIMENTAL SECTION

Materials. Protease from *A. oryzae* (≥500 U g^{-1}), α-amylase from *A. oryzae* (≥30 U mg^{-1}), sodium acetate, acetic acid, hydrochloric acid, sodium hydroxide, DMSO-d_6, glycogen from oyster (OG), rabbit liver (RLG), and bovine liver (BLG), trifluoroacetic acid (TFA), concentrated sulfuric acid, phenol, DMSO, DMF, and ethanol were purchased from Sigma-Aldrich and used without further purification. Glycogen from sweet corn (phytoglycogen; PG) was purchased from Glysantis Inc. (Canada) and used without further purification. NIPAM was purchased from Sigma-Aldrich and purified by recrystallisation twice in hexane before use. A Pierce BCA protein assay kit was purchased from Thermo Fischer Scientific. Fluorescence labeling of the particles was performed using AF488-NHS, purchased from Thermo Fisher Scientific (MA, USA), and 4-(dimethylamino)pyridine (DMAP) purchased from Merck (Munich, Germany). Quantitative thiol content determination was performed using a fluorometric free thiol assay kit purchased from Abcam (Cambridge, UK). Lysis of red blood cells (RBC) was performed using Pharm Lyse buffer from BD Biosciences (Heidelberg, Germany). For cell phenotyping, antibodies against CD3 AF700 (SP34-2), CD11b Pacific Blue (ICRF44), CD14 APC-H7 (MΦP9), CD66b BV421

(G10F5), CD45 V500 (HI30), CD56 PE (B159), lineage-1 cocktail APC, HLA-DR PerCP-Cy5.5 (G46−6), and CD19 BV650 (HIB19) were used, all purchased from BD Biosciences, except for lineage-1 cocktail, CD15 and CD19 that were obtained from BioLegend (CA, USA). Purification following phenotyping was performed using FACS buffer (PBS buffer containing 0.5% w/v bovine serum albumin, purchased from Merck, and 2 mM ethylenediaminetetraacetic acid purchased from Thermo Fisher Scientific). Cell fixation was performed using formaldehyde (1% w/v), which was purchased from Merck and diluted in PBS. C5a concentration was determined using an enzyme-linked immunosorbent assay (C5a ELISA from DRG Diagnostics, Marburg, Germany). The pH of the solutions was measured by a Mettler-Toledo MP220 pH meter. Milli-Q water with a resistivity greater than 18.2 MΩ cm was used in all experiments and obtained from a three-stage Millipore Milli-Q plus 185 purification system (Millipore Corporation, USA).

OG-PNIPAM Synthesis. OG (100 mg) was dissolved in DMSO (2 mL) and Milli-Q water (1.4 mL and 0.8 mL for OG-PNIPAM 1 and OG-PNIPAM 2, respectively) in a 10 mL Schlenk tube with a magnetic stirrer bar. Milli-Q water was added to ensure complete dissolution of the OG nanoparticles. NIPAM (234 mg) was dissolved in DMF (1 mL) and the resulting solution was added to the OG solutions. The Schlenk tube was sealed with a rubber septum and then subjected to three consecutive freeze–pump–thaw cycles to remove oxygen. The system was then flushed under argon and subsequently sealed. Photopolymerization was then performed by irradiation with UVA light for 24 h while the OG/NIPAM solution was continuously stirred. After the reaction was stopped, the crude product was precipitated in cold ethanol, isolated by centrifugation (3000 *g*, 5 min), washed two times with cold ethanol to remove excess monomers, dispersed in Milli-Q water, and then freeze-dried overnight. OG-PNIPAM 1 (yield 72 mg). OG-PNIPAM 2 (yield 53 mg). ^{1}H NMR (400 MHz, DMSO-d_6): δ = 5.48 (s, 1H), 5.05 (s, 0.6H), 4.89 (s, 0.3H), 4.54 (s,

0.7H), 3.92–3.25 (m, 8H), 3.08 (s, 0.07H), 1.25 (s, 0.07H), 1.04 (m, 0.3H and 0.05H for OG-PNIPAM 2 and OG-PNIPAM 1, respectively).

In Situ Protease Digestion. OG (5 mg) was dissolved in 50 mM acetate buffer (1 mL, pH 5.0) with gentle sonication. The sample was placed in a glass DLS cuvette, covered, and heated to 45 °C. Once equilibrated for 5 min, a set of sequential DLS measurements were commenced (staggered in time by 10 s), with protease (2 μL) from *A. oryzae* rapidly added and mixed after the first measurement. Size distributions were then measured over the following 35 min.

Isolation of OG-PNIPAM Post Protease Digestion. A sample of OG-PNIPAM 2 (12 mg) was dissolved in Milli-Q water (250 μL) to which protease (2 μL) was added, and the solution was stirred at 23 °C for 8 h. The crude product was then precipitated in cold ethanol, isolated by centrifugation (5000 *g*, 10 min), washed two times with cold ethanol, dispersed in Milli-Q water, and then freeze-dried overnight (yield 7 mg).

Degradation of Particles by α-Amylase. The enzymatic degradation of OG, OG-PNIPAM 1, and OG-PNIPAM 2 was assessed using a phenol-sulfuric acid assay.[27, 42] Solutions of each particle type were prepared in Milli-Q water at a concentration of 2 mg mL^{-1} and a solution of α-amylase in PBS buffer (1.0 U mL^{-1}, pH 7.4) was prepared. To begin the assay, a glycogen solution (70 μL) was added to the enzyme solution (200 μL), and the resulting solution was incubated at 23 °C with gentle agitation for 3 h. Then, the undigested glycogen and enzyme were separated from the free glucose using spin columns with a pore size of 10 kDa (Amicon Ultra Centrifugal Filter Unit, Sigma-Aldrich). The filtrate was collected and divided into sample aliquots of 50 μL, to which concentrated sulfuric acid (150 μL) was added, followed by addition of 5% phenol solution (30 μL, v/v in water). The samples were subsequently incubated at 90 °C with agitation for 5 min. The UV–Vis absorbance of the digested solution was then measured at 490 nm with an Infinite M200

microplate reader (Tecan, Switzerland) using a 96-well plate (Greiner CELLSTAR, Sigma-Aldrich). To determine the amount of glucose on each particle type, the original glycogen solutions (70 μL) were each treated with of 0.2 M TFA (200 μL) for 3 h at 80 °C with agitation. The mixtures were then treated and analyzed as described above for the enzymatic experiments. The extent of degradability was determined as the ratio of the UV–Vis absorbance reading intensity at 490 nm for the enzymatically degraded particles to the acid-degraded particles.

SEC-SAXS. SEC-SAXS analysis was performed at the SAXS/WAXS beamline of the Australian Synchrotron using a Shimadzu LC20 HPLC.[43-44] The Milli-Q eluant from a series of ultrahydrogel columns (1× 250 Å, 1× 2000 Å, 1× guard column), purchased from Waters, was directed through the X-ray beam via a 1 mm fixed quartz capillary (using co-flow[45] at a sample-to-total flow rate ratio of 1:2) at a sample flow rate of 0.5 mL min^{-1}. SAXS images were acquired using an exposure interval of 5 s and a Pilatus2-1M detector, with a sample-to-detector distance of 7 m and a photon energy of 12 keV. All two-dimensional SAXS images were normalized to beamstop measured beam transmission, absolute scaled to water scattering, and reduced to one-dimensional scattering profiles using scatterBrain v2.82. Deconvolution and SVD analysis were conducted using UltraScan-SOMO[46] with plain Gaussian distributions; Guinier analysis, $P(r)$ analysis, and de novo shape reconstruction were conducted using DATRG, GNOM,[47] and DAMMIF[48] from the ATSAS suite[49] of the SAXS analysis tools.

NMR. The ^{1}H (500.13 MHz) NMR spectra were recorded using an Avance III 500 spectrometer (Bruker, Germany) using DMSO-d_6 as solvent at 30 °C.

GPC. Molecular weight determination was performed using an Agilent Technologies 1260 Infinity HPLC system, equipped with a PL aquagel OH-mixed-H column purchased from Agilent Technologies connected to a refractive index detector K-2301 (Knauer), a UV-detector 2520

(Knauer), and a miniDAWN-LS TREOS II (Wyatt Technologies). A mixture of 10 mM NaH_2PO_4 (pH = 7) and 0.2 M $NaNO_3$ was used as the eluent with a flow rate of 1 mL min^{-1}.

TEM. TEM images were acquired on a Libra 120 cryo-transmission electron microscope (Carl Zeiss NTS GmbH) equipped with a LaB_6 source. The acceleration voltage was 120 kV. The samples were prepared by dropping the test solution (0.3 mg mL^{-1} in Milli-Q water) onto a carbon-coated copper grid (CF200-Cu, Electron Microscopy Sciences, Hatfield, PA, USA). After 2 min, the solution was removed by blotting with a filter paper.

AFM. Liquid-state AFM was performed in Milli-Q on a Cypher instrument (Asylum Research, USA) equipped with a sample heating stage. Images were acquired in tapping mode using BioLever Mini (BL-AC40TS) cantilevers (Oxford Instruments, USA). In water, the cantilevers were driven with the Blue Drive technology. Dry-state AFM was performed with a JPK NanoWizard II BioAFM instrument. Scans were conducted in intermittent contact mode with MikroMasch silicon cantilevers (NSC/CSC).

DLS and ζ-Potential. All DLS and ζ-potential measurements were performed using a Malvern Zetasizer instrument fitted with a 4 mW He-Ne laser (633 nm).

Fluorescence Labeling of OG-Based Particles. To fluorescently label the particles, AF488-NHS was reacted with the hydroxyl groups of the glycogen particles. The particles were dispersed in DMSO (anhydrous, 400 μL) with DMAP (0.5 mg) present. AF488-NHS (16 μL, 1 mg mL^{-1} in anhydrous DMSO) was added. After 2 h at 20 °C under constant shaking, unreacted dye was removed using Vivaspin centrifugal concentrators (molecular weight cut off (MWCO) 100 kDa, Merck). The particles were centrifuged (12000 *g*, 5 min), washed with Milli-Q water (2×), freeze-dried, and stored in the fridge (~8 °C) in the dark prior to use.

Thiol Assay. Fluorometric thiol group determination was performed following a standard protocol provided by the supplier. The particles (4 mg) were dissolved in the reaction buffer (200 µL) (provided by the supplier). A glutathione (GSH) reaction mixture (200 µL) (20 µL, 100× diluted (reaction buffer) thiol green indicator (TGI) stock solution (100× in DMSO (anhydrous)) was added to the particle dispersion prior to centrifugation (12000 *g*) using Vivaspin centrifugal concentrators (MWCO 100 kDa). Samples were collected after 17, 25, and 50 min of centrifugation and analyzed using a multimode microplate reader (Tecan Spark 10M, Switzerland, excitation wavelength λ_{exc} = 490 nm, emission wavelength λ_{em} = 520 nm). Thiol group concentrations were determined via comparison to a GSH standard curve.

Assays Using Human Blood and Derivatives. All studies were approved by the ethics board and complied with institutional and international guidelines (review board of Sächsische Landesärztekammer, Germany). All blood donors provided informed consent and did not use any medication 10 days prior of the experiment. Studies were performed with triplicates of each sample. Fresh venous blood was collected from a healthy human volunteer into sodium heparin vacuettes (Greiner Bio-One) or heparin pre-loaded syringes (1 U mL^{-1} heparin, Ratiopharm, Ulm, Germany). A point-of-care assay for C-reactive protein (CRP, Diagnostik-Nord, Schwerin, Germany) and a differential blood cell count (ACTdiff, Beckman Coulter, Germany) (Table S2) were determined before performing subsequent tests. Blood samples were excluded if they showed any signs for inflammation. Experiments commenced within 15 min of blood collection. To prepare washed blood, the blood cells with plasma removed were first topped up with PBS (45 mL) and centrifuged at 950 *g* for 10 min, with slow brake. The supernatant was removed, and this wash step was repeated four times. The absence of plasma proteins was confirmed by the lack of absorbance of the PBS supernatant of washed blood at 280 nm (Nanodrop ND-1000, peQLab

Biotechnology, Germany). Before and after blood separation and washing steps, the white blood cell count was kept constant within the limits of the experimental conditions (Table S2).

Blood Assay to Measure Association of Particles with Human Immune Cells. Blood assays were performed following a recently published protocol.[50] The particles (250 μg) were incubated in whole blood (100 μL) or washed blood (100 μL) for 1 h at 37 °C. RBC were lysed by adding Pharm Lyse buffer at 40× blood volume and washed with Dulbecco's phosphate-buffered saline (DPBS; 4 mL, 2×) (500 *g*, 5 min, 4 °C). Cells were phenotyped on ice for 1 h using antibodies against CD3 AF700 (SP34-2), CD14 APC-H7 (MΦP9), CD66b BV421 (G10F5), CD45 V500 (HI30), CD56 PE (B159), lineage-1 cocktail APC, HLA-DR PerCP-Cy5.5 (G46−6), and CD19 BV650 (HIB19). Unbound antibodies were removed by washing and centrifugation (500 *g*, 5 min, 4 °C) with FACS buffer. Cells were fixed in 1% w/v formaldehyde in PBS. The samples were directly used for cell association analysis by flow cytometry (LSRFortessa, BD Biosciences, USA) and analyzed using BD FACSDiva Software.

Blood Assay to Measure the Hemocompatibility of OG-based Particles. A Chandler loop setup was used to mimic in vivo the shear conditions.[16] Tygon silicone tubes (type 3350, internal diameter 3.2 mm, length 55 cm) were cleaned repeatedly with ethanol and Milli-Q water in an ultrasound bath, before being filled with 3 mL of heparin-anticoagulated blood containing a particle concentration of 200 μg mL^{-1}. The tubes were closed to a loop and mounted on a vertical rotating disc (13 rpm, which converts to a blood flow rate of 17 cm s^{-1} and an estimated wall shear stress of 0.18 Pa)[51] to incubate for 1 h at 37 °C. Following incubation, the blood was analyzed with regards to CD11b expression on neutrophils and C5a formation. C5a concentration was determined by ELISA from EDTA anticoagulated plasma. Neutrophil activation was measured by flow

cytometry (LSRFortessa, BD Biosciences, USA) and analyzed using BD FACSDiva software following neutrophil staining using Pacific Blue labelled anti-CD11b.

Minimum Information Reporting in Bio-Nano Experimental Literature. The studies conducted herein, including material characterization, biological characterization, and experimental details, conform to the MIRIBEL reporting standard for bio-nano research,[52] and we include a companion checklist of these components in the Supporting Information.

RESULTS AND DISCUSSION

Protein Component of Glycogen Nanoparticles. In vivo, glycogen nanoparticles are associated with a population of proteins that mediate its biological functions, including management of glucose addition and cleavage from the particles, regulation of particle size, concentration, and cellular location.[53] Two key enzymes in glycogen synthesis are glycogen synthase, which is responsible for the bulk synthesis of glycogen by formation of the α-1,4-glycosidic linkages, and the glycogen-branching enzyme, which cuts the distal end of a newly formed chain and re-attaches it to a glucose residue from an older chain as an α-1,6-glycosidic linkage (Figure 1).[19, 54-55] The biosynthesis of glycogen is initiated by a priming protein glycogenin, which exists as different isoforms depending on the cell type. Glycogenin auto-glycosylates oligosaccharide chains of glucose of approximately 7–12 units long,[56] which is then used as a starting point from which other enzymes grow the glycogen particles in a bottom-up approach.[54] Glycogenin also plays a role in regulating glycogen size and quantity[57] and is involved in the formation of supramolecular glycogen nanoparticles (so-called α-particles).[39] These studies suggest that the protein component of glycogen may be either incorporated within the structure or/and situated on the surface of the particles. However, details on the role of the protein component in preserving the structure of glycogen nanoparticles are lacking in the literature,

particularly because of existing challenges in probing the presence of proteins on "soft" nanoparticles.

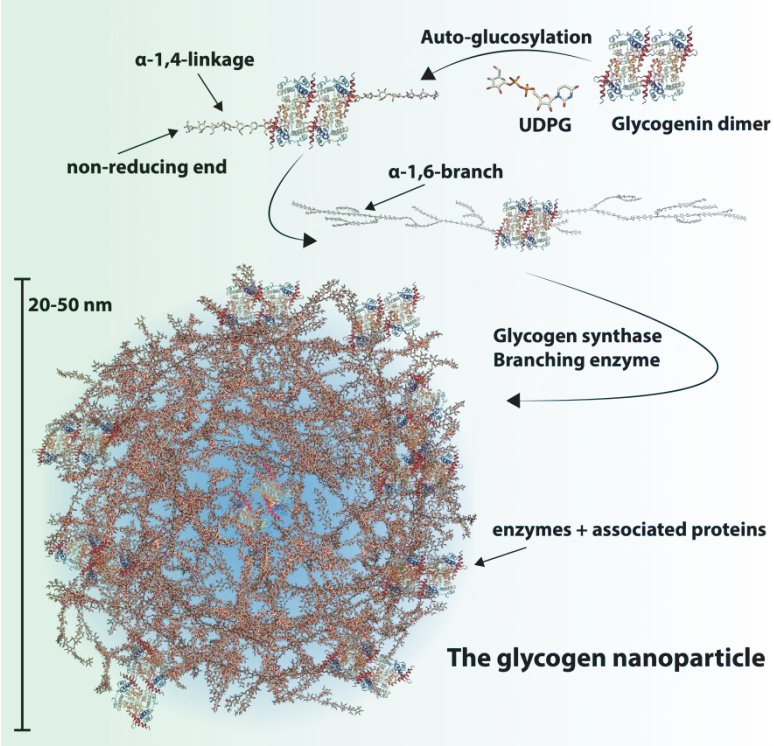

Figure 1. Reaction scheme describing the biological synthesis of glycogen from the protein core. UDPG, uridine diphosphate glucose. Reprinted in part with permission from ref. 24. Copyright 2019 John Wiley and Sons.

There are four common commercial sources of glycogen, namely OG, rabbit liver glycogen (RLG), bovine liver glycogen (BLG), and phytoglycogen (PG). The protein component that remains covalently bound to each glycogen particle type (derived from the aforementioned glycogen sources) was probed by a bicinchoninic acid (BCA) assay. OG featured the largest amount of accessible protein per mass of nanoparticles (Figure 2A) at ~8 μg of protein per mg of glycogen, followed by BLG (5.3 μg mg^{-1}), RLG (2.9 μg mg^{-1}), and PG (1.6 μg mg^{-1}). The quantity of protein in Figure 2A is of the same magnitude to that previously determined by a Bradford assay

for non-degraded liver glycogen isolated from healthy rats and mice.[58] Herein, OG was used for the subsequent studies owing to the high protein content. To examine the role of the protein in maintaining the structural integrity of the nanoparticles, OG was incubated with protease from *Aspergillus oryzae* (*A. oryzae*). The nanoparticle size was monitored in situ by dynamic light scattering (DLS). After incubation for 35 min, the peak of the intensity size distribution shifted from ~50 nm to ~40 nm (Figure 2B). This shift indicated that protease successfully cleaved the protein component from the glycogen nanoparticles, leading to an increase in the distribution of smaller nanoparticles. To gain further insights into the nature of the protease digestion, the nanoparticles before and after digestion were subjected to SAXS analysis following inline SEC separation of the particles based on their hydrodynamic size. As noted in the SEC profiles shown in Figure 2C, there was a distinct shift in the elution time of the OG particles following protease digestion relative to the SEC profile of OG. The average radius of gyration, r_g, of the particles was determined at each point in the SEC profile from Guinier analysis of the SAXS scattering data at low q. Each corresponding point between the profiles (i.e., matching elution time) gave similar r_g values although there were fewer larger particles present in the protease-digested OG sample.

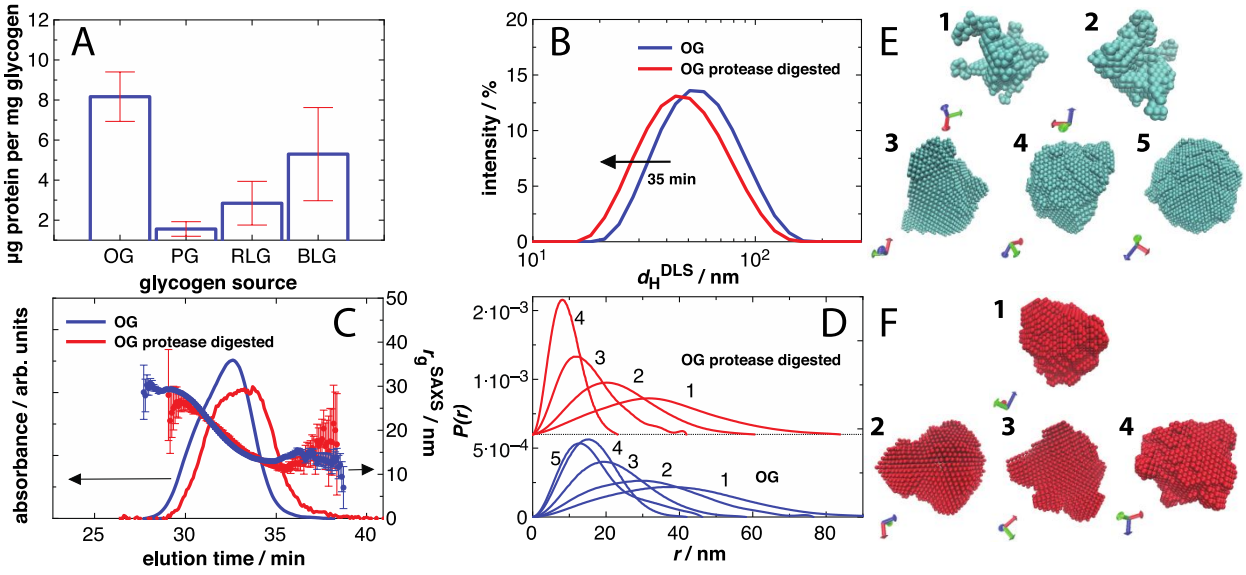

Figure 2. (A) Protein assay of the amount of protein per mass of glycogen for four different glycogen sources (OG, oyster glycogen; PG, phytoglycogen; RLG, rabbit liver glycogen; BLG, bovine liver glycogen). Error bars represent standard deviations (n = 3). (B) DLS intensity distributions before (blue) and after (red) protease treatment in 50 mM acetate buffer (pH 5.0) at 45 °C (n = 1). d_H^{DLS}, DLS hydrodynamic diameter. (C) SEC profiles and corresponding r_g^{SAXS} as determined from Guinier analysis of the SAXS scattering profiles (right axis) before (blue) and after (red) protease digestion treatment (n = 1). Error bars represent the standard error in r_g^{SAXS} from the fits to the SAXS profiles. (D) $P(r)$ profiles of OG and protease-digested OG from the SAXS profiles for selected regions in the SEC profiles (see Supporting Information). Note these distributions are normalized by area and offset for clarity, and the quantity "r" represents the distance between electrons across the particles that is different from the radius of gyration, r_g. DAMMIF shape reconstructions for the $P(r)$ profiles of (D) are shown for each peak of the (E) OG and (F) protease-digested OG samples.

Single-value decomposition (SVD) was used to fit the SEC profiles to individual distributions of particles, where the OG particles were fitted to five distributions and the protease-digested OG particles were fitted to four distributions (Figure S1A). The peak of each distribution was then used as a basis to compare the average particle properties from the SAXS data for each individual distribution of particles by comparing changes in the pair distribution functions, $P(r)$, between the systems. The $P(r)$ functions provide the distribution of all distances between electrons within a sample. This therefore provides an indication of particle shape before and after incubation of the OG nanoparticles with protease. The $P(r)$ functions (Figure 2D) revealed that each distribution contained particles of similar shape but different size. A reduction in the longer-range components

of the first population in the digested sample relative to the OG sample was observed, as well as a reduction in the "shoulder" components toward larger distances of the smaller populations. These shoulder components reflect a slightly elongated shape for some glycogen nanoparticles.[38] Shape reconstructions were generated for each of the peak of the distributions in Figure 2D with the program DAMMIF,[48] which are shown in Figure 2E and F. The larger particles in OG were less homogeneous in shape, particularly for distributions 1 and 2, whereas the smaller distributions converged to more spherical particles. Comparison of the OG and protease-digested OG reveals that the protease-digested sample is, on average, more spherical across all distributions. This was confirmed by further analysis of the inertia tensor for each mass of coordinates (Table S1), where the OG particles had one or two axes that had a lower principal moment of inertia than the other orthogonal axes, reflecting slightly elongated or oblate particles. In contrast, the protease-digested sample had similar eigenvalues across most distributions besides distribution 1, which reflects the presence of more spherical-like particles. These results show an increase in the quantity of smaller spherical particles upon digestion with the protease *A. oryzae*, suggesting removal of surface-bound proteins. It is anticipated there are other glycogen-associated proteins that are embedded within the particle. However, the glycogen-associated protein exposed on the surface, which is accessible to protease enzymes, may influence the biological behavior of the glycogen nanoparticles and potentially can be exploited for further functionalization.

Photopolymerization from Protein Moieties. We explored the potential to exploit the protein moieties for tuning the structural and functional properties of glycogen nanoparticles. Recently, Goldhahn et al.[59] reported the protein-initiated photopolymerization of NIPAM from the thiol groups of bovine serum albumin-coated gold nanoparticles. This method is highly advantageous over traditionally employed atom transfer radical polymerization as it does not require transition

metal catalysts (i.e., copper(I) complexes), ligands, or modification of the protein coating with an initiator.

Specifically, herein, the use of the protein that is inherently part of OG nanoparticles was examined toward the polymerization of NIPAM from glycogen (Figure 3A). Glycogen nanoparticles lack an intrinsic thermo-responsiveness at biologically relevant temperatures but have been shown to slightly degrade upon prolonged heating at 80 °C.[60] It is envisioned that by growing thermoresponsive PNIPAM chains from the protein component of glycogen, a temperature responsiveness can be endowed to the particles at biologically relevant temperatures. Furthermore, the inclusion of PNIPAM may provide switchable surface properties in terms of hydrophobicity of the glycogen nanoparticles.

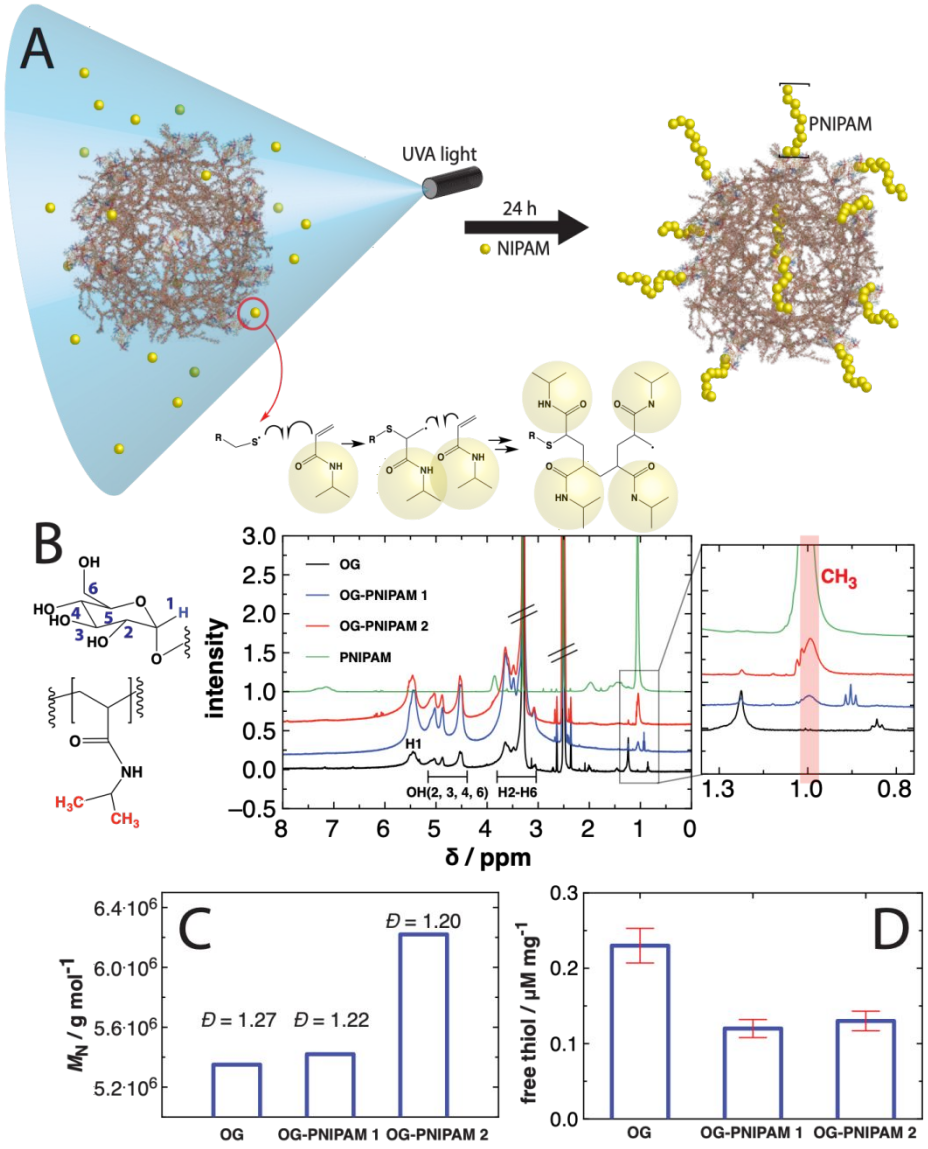

Figure 3. (A) Schematic describing the thiol-initiated photopolymerization of NIPAM from the protein component of glycogen nanoparticles. (B) ^{1}H NMR spectra measured in DMSO-d_6 at 25 °C of OG, OG-PNIPAM 1, OG-PNIPAM 2, and a linear PNIPAM polymer (M_N = 13 kDa) for reference (the crossed lines indicate solvent). (C) GPC results showing the M_N of each particle type along with the polydispersity $Đ = M_W / M_N$ (n = 1 for each particle type). (D) Amount of free thiol present in each particle system. Error bars represent standard deviations (n = 3).

For the synthesis, OG nanoparticles were first dispersed in a mixture of dimethyl sulfoxide (DMSO) (2 mL) and Milli-Q water (1.4 mL and 0.8 mL for OG-PNIPAM 1 and OG-PNIPAM 2, respectively), to which a solution of NIPAM in *N*,*N*-dimethylformamide (DMF) (1 mL) was mixed. Milli-Q water was added in different amounts to create a particle concentration difference between the two systems and to facilitate the complete dissolution of the glycosidic chains within glycogen to expose the greatest amount of protein. Bertoldo et al.[61] have previously shown that when glycogen is present in organic solvents, most functionalization is limited to the "external shell" of the surface of the nanoparticles. Following removal of oxygen by three consecutive freeze–pump–thaw cycles, the system was then left under argon with rigorous stirring and irradiated with UVA light (320 nm < λ < 420 nm) for 24 h at 23 °C. During this process, the UVA light generates thiyl radicals from thiol groups, which initiate the free radical photopolymerization of NIPAM directly from the particles (Figure 3A).[59] The purified particles were subsequently analyzed and compared to OG by ^{1}H nuclear magnetic resonance (NMR) spectroscopy in DMSO-d_6 at 25 °C (Figure 3B). The spectra of all three particle systems featured the signature peaks of glycogen, namely the key reference of the H1 proton at ~5.5 ppm. Importantly, at ~1.05 ppm, a new peak was seen for both OG-PNIPAM samples, which is the signature CH_3 peak of PNIPAM, which is distinct from the D-glucose peaks.[62] The magnitude of this peak was greater for OG-PNIPAM 2 than for OG-PNIPAM 1, reflecting that OG-PNIPAM 2 was synthesized from a solution of smaller volume (greater concentration of nanoparticles), which resulted in a greater amount of PNIPAM on the OG nanoparticles. This was confirmed by repeating the synthesis at two intermediate volumes, which was achieved by variation of the volume fraction of water (all else remaining the same). It was found that the trend was consistent for a greater amount of PNIPAM conjugated for higher particle concentration systems (Figure S2).

Gel permeation chromatography (GPC) was performed on all particle types to determine the molecular weights of OG-PNIPAM 1 and OG-PNIPAM 2. An increase in the molecular weight was observed for both samples (Figure 3C), relative to that of OG, i.e., ~2% for OG-PNIPAM 1 and ~17% for OG-PNIPAM 2, which emphasizes the strong difference in polymerization conditions based on concentration in solution. The polydispersity was similar for all samples, even slightly reduced for OG-PNIPAM 2 compared to OG, indicating that the synthesis does not widen the distribution of particles. The GPC light scattering traces show that there are no additional PNIPAM species that are not conjugated to the glycogen nanoparticles (Figure S3). To clarify the nature of the conjugation of PNIPAM to the particles, a thiol assay was performed to determine the amount of free thiol groups on each particle system. We point out that the assay does not reveal information on the total presence of thiol species in the particle systems, only amount of free thiol (i.e., disulfide conjugations are not detected). Nonetheless, the assay should provide a qualitative measure of change due to the polymerization. Following polymerization, a reduction of ~50% in the amount of free thiol groups on the particles was observed (Figure 3D) in both OG-PNIPAM 1 and OG-PNIPAM 2. This result indicates that despite the presence of a different amount of PNIPAM on the particles, the degree of surface initiation is similar, suggesting the presence of longer PNIPAM chains in OG-PNIPAM 2.

Transmission electron microscopy (TEM) and dry-state atomic force microscopy (AFM) analyses were performed on OG-PNIPAM 2 to determine the dispersity and size of the particles. As observed from Figure 4A, the particles were well dispersed with a dry diameter greater than the hydrodynamic diameter (DLS, Figure S4). This result reflects the soft nature of the particles, where they flatten in the perpendicular dimension to the surface upon removal of the solvent. Additionally, from the TEM image (Figure 4A) some particles appeared to feature spherical sub-

structures, which are attributed to the original glycogen particles where the outer structure is potentially the PNIPAM chains. The OG-PNIPAM 2 particles were found to be denser in appearance than the OG starting material (Figure 4B), which is typically difficult to visualize in the absence of staining reagent. Furthermore, AFM imaging of OG-PNIPAM 2 (Figure 4C) shows a low-definition corona around the surface (lower contrast), likely indicating the surface-bound PNIPAM and glycosidic chains.

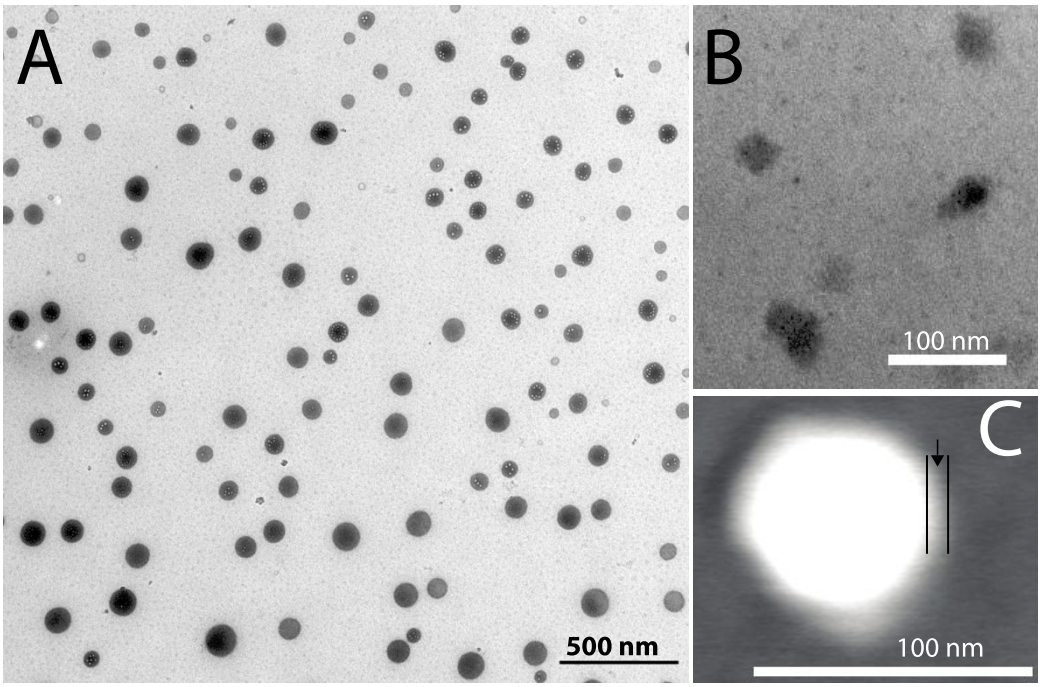

Figure 4. TEM images of OG-PNIPAM 2 (A) and OG (B) particles dispersed on a copper grid, and a dry-state AFM image (C) of a single OG-PNIPAM 2 particle showing the soft edge of the particle (indicated by the arrow enclosed within the black lines).

Given the presence of PNIPAM on the particles, it is expected that the OG-PNIPAM particles are endowed with a temperature responsiveness with respect to their colloidal stability. DLS measurements were performed on each particle type in Milli-Q water, where the sample-containing cuvette was heated from 20 to 60 °C at 2 °C increments with an equilibration time of 7 min before

the DLS measurements were performed (Figure 5A). Upon heating to temperatures above the lower critical solution temperature (LCST) of PNIPAM (32 °C), the average particle size of both OG-PNIPAM systems increased rapidly. This increase was dependent on particle concentration, with larger increases achieved for more concentrated particle dispersions (10 vs 1 mg mL^{-1}), indicating a controlled aggregation phenomenon. For a given concentration, for example, of 10 mg mL^{-1}, the extent of increase in particle size with increases in the temperature was larger for OG-PNIPAM 2 than for OG-PNIPAM 1. The particle size of OG-PNIPAM 2 increased from approximately 43 to 80 nm with a temperature range of 20 °C (from 28 to 48 °C), whereas that of OG-PNIPAM 1 increased from approximately 39 to 56 nm within the same temperature range. This result likely reflects the greater influence of the higher number average molecular weight (M_N) of PNIPAM on the OG-PNIPAM 2 particles (Figure 3C). In contrast, OG did not show an increase in particle size as a function of temperature. A slight decrease in the hydrodynamic size with increasing temperature was observed for OG, likely reflecting an increase in the mobility of the particles at higher temperatures. The nature of the aggregation was assessed by DLS intensity distributions (Figure 5B). Below the LCST, a monomodal distribution was observed, whereas at 60 °C, a bimodal distribution was observed, indicating the presence of larger particle aggregates of ~200 nm. The aggregate size was tunable; the smaller aggregate size could be recovered upon cooling the sample to 25 °C (Figure 5B).

Prior to the DLS measurements (Figure 5A and B), the samples were allowed to equilibrate at each sequential temperature between 20 and 60 °C for 7 min. Thus, for each temperature measurement taken, the particles reached an equilibrium aggregate size. This was confirmed by monitoring the average particle size as a function of time at different temperatures (Figure 5C)—the average size stabilized promptly once the set temperature was reached. This result indicates

that the temperature-driven aggregation of the particles can be finely controlled by both the temperature and particle concentration in solution.

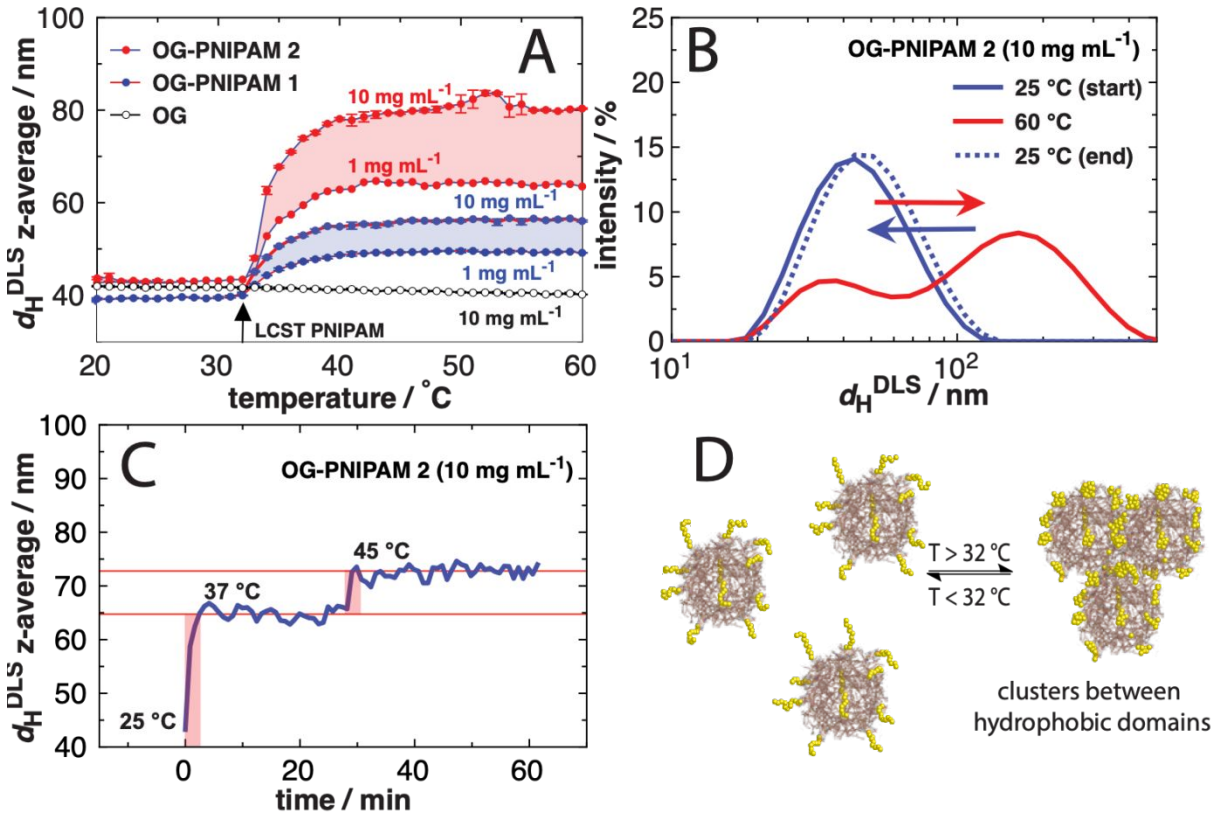

Figure 5. (A) DLS measurements of the variations in the *z*-average diameter of OG (10 mg mL^{-1}), and OG-PNIPAM 1 and OG-PNIPAM 2 (1 and 10 mg mL^{-1}) as a function of temperature and concentration. Error bars represent standard deviations ($n = 3$). (B) DLS intensity distributions of OG-PNIPAM 2 at 10 mg mL^{-1} as the temperature was varied from 25 °C (start) to 60 °C and 25 °C (end) ($n = 3$). (C) Variations in the *z*-average diameter, measured by DLS, of OG-PNIPAM 2 (10 mg mL^{-1}) as a function of time after heating to 37 °C and then to 45 °C. The red vertical bars indicate the period where heating took place, whereas the red horizontal lines indicate variations in the average diameter over the time period at 37 °C and 45 °C ($n = 1$). (D) Schematic describing the aggregation of OG-PNIPAM particles with variations in the temperature.

To topographically image the temperature-induced change in size of the individual nanoparticles, liquid-state AFM of the nanoparticles deposited on freshly cleaved mica was performed. Upon increasing the temperature from 25 to 40 °C at 3 °C increments, the particle size in the *z*-dimension perpendicular to the surface (Figure 6A and D) decreased from ~45 nm to ~33 nm. The largest decrease in size occurred around the LCST of PNIPAM, which indicates collapsing of the PNIPAM chains onto the particles. Similar results have previously been reported for PNIPAM microgel particles that exhibit volume changes due to temperature changes around the LCST of PNIPAM.[63] Upon cooling the system to the starting temperature, the average particle size reverted to ~44 nm. The same experiment was repeated in air (Figure 6B and S5), where a smaller trend with temperature changes was observed, as the phase transition is driven by the hydrophobic effect, but smaller particles (size difference of up to 30 nm) were observed relative to the fully solvated particles. This result highlights the hydration property of glycogen in the presence of water. As previously reported by Nickels et al.,[64] OG nanoparticles contain between 250% and 285% of their mass in water. The ζ-potential of the OG-PNIPAM 2 particles was relatively independent of temperature; a slight reduction from approximately −12 mV to approximately −10 mV was noted as the temperature was increased from 25 °C to 65 °C (Figure 6C). The negative charge is indicative of a small amount of phosphate on the particles that remains from biological synthesis and degradation processes.[24] The independence of the ζ-potential with temperature indicates that the PNIPAM chains do not shield the native charge of glycogen. Dry-state AFM images of the OG-PNIPAM 2 nanoparticles on a silicon wafer (Figure 6G–I) show a higher contrast in phase around the edges of the particle in comparison to the centre of the particle, indicative of the presence of collapsed PNIPAM chains around the edges. These data suggest that the collapse of the PNIPAM chains onto the particles at temperatures above the LCST changes the

colloidal stability of the particles to a more "hydrophobic" species. This subsequently causes the particles to aggregate (Figure 5D), of which the extent can be controlled.

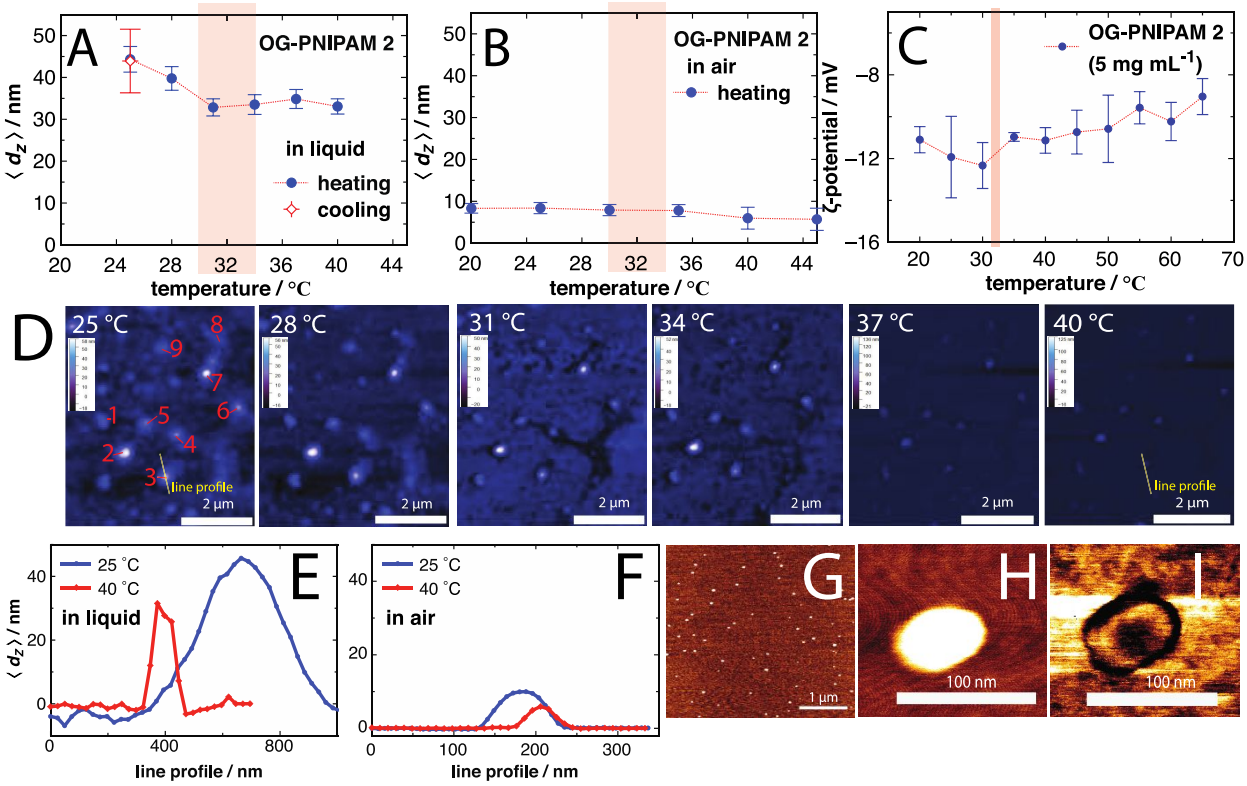

Figure 6. Relative height of the OG-PNIPAM 2 particles as a function of temperature determined from atomic force microscopy (AFM) topographic imaging conducted in (A) a liquid and (B) air environment of the particles adsorbed onto freshly cleaved mica. Error bars represent standard deviations (n = 9). (C) Variations in the ζ-potential of OG-PNIPAM 2 as a function of temperature when dispersed in Milli-Q water. Error bars represent standard deviations (n = 3). (D) In-liquid AFM topographic images corresponding to the data in (A), where nine particles were monitored across all temperatures, along with line profiles (yellow lines in D) for single particles at 25 °C and 40 °C in liquid (E) and air (F) (n = 1). (G) In-air tapping mode AFM imaging of OG-

PNIPAM 2 dispersed on a silicon wafer, and associated images of a single particle recorded in (H) standard and (I) phase-contrast modes.

The grafted PNIPAM onto the protein component of glycogen is expected to be removed once the protein is biodegraded. To evaluate this, OG-PNIPAM 2 was incubated with protease for 12 h. Following purification and isolation, the intensity of the peak corresponding to the PNIPAM CH_3 protons decreased considerably in the ^{1}H NMR spectrum of OG-PNIPAM 2 (Figure S6) following protease treatment. Furthermore, as revealed by the DLS temperature study, the OG-PNIPAM 2 particles after protease treatment no longer displayed temperature responsiveness and the average particle size remained unchanged between 20 and 60 °C (Figure 7A). Importantly, these results clarify the nature of the PNIPAM conjugation to the OG particles, showing that once the protein is removed, so is the PNIPAM component. In addition, this demonstrates that enzymatic degradation of the protein component of the particles is not inhibited in the presence of PNIPAM. Further enzymatic degradation was confirmed by subjecting all particle systems to an α-amylase digestion assay (Figure 7B); all particles types displayed comparable degradability by α-amylase from *A. oryzae*. The addition of a temperature-responsive functionality therefore did not change the relative biodegradability of the particles, indicating that PNIPAM does not inhibit access of the amylase to the exposed surface chains for degradation, or protease from the surface protein component. In vivo, there are numerous other glucosidase enzymes that may degrade the particles. Thus, the degradation data shown in Figure 7B are only reflective of degradation by one specific enzyme.

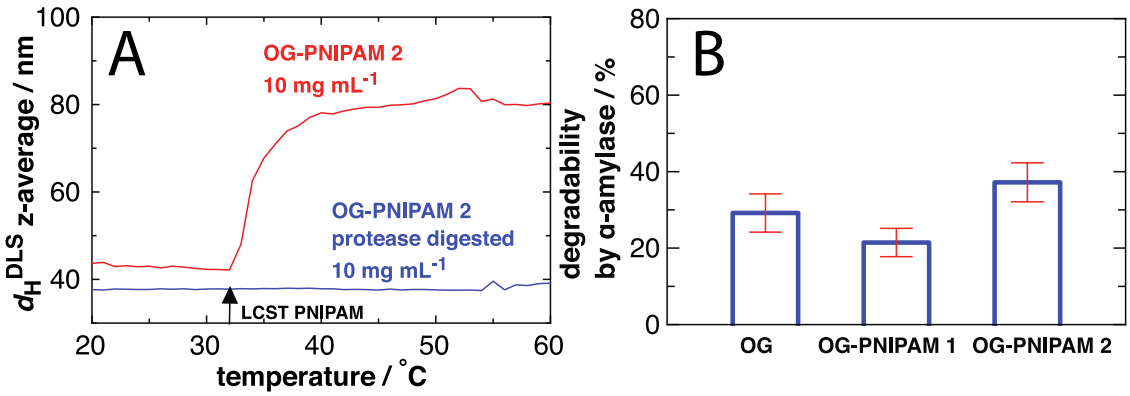

Figure 7. (A) Comparison of the temperature responsiveness of the OG-PNIPAM 2 particles before (red) and after (blue) protease digestion, as assessed by DLS measurements in Milli-Q water. LCST, lower critical solution temperature. (B) α-Amylase degradation assay to determine the biodegradability of the OG and OG-PNIPAM particles. Error bars represent standard deviations (n = 3).

Interaction of OG-PNIPAM in Biological Contexts. The functionality endowed to the OG particles through PNIPAM offers potential application in aggregation-based drug or gene encapsulation,[27] or for tuning the interaction of the OG particles toward different solutes and interfaces.[59] From a physiological standpoint, it is important that the natural hemocompatibility and stealth character of the OG nanoparticles with immune cells is not compromised by the additional PNIPAM component on the particles (i.e., that some of the benefits of using glycogen nanoparticles for physiological applications are not lost through the functional motifs). The surface hydrophobicity and charge,[65-66] as seen for octenyl succinate-modified glycogen,[29, 40] influence the interaction of nanoparticles with immune cells and therefore the outcome in physiological environments. We have previously shown that glycogen nanoparticles are relatively low fouling in the presence of fetal bovine serum[26] and that glycoplexes composed of glycogen and siRNA molecules have a considerably long circulation lifetime of approximately 8 h in healthy mice.[27]

The interaction of OG and the OG-PNIPAM systems with human immune cells was investigated by performing human blood association assays. Human blood assays mimic a highly complex, biologically relevant microenvironment, wherein particle–cell interactions occur simultaneously with the formation of a biomolecular corona. The assays allow identification of the cell type (neutrophils, monocytes, dendritic cells, B cells, T cells, natural killer (NK) cells) associating with the nanoparticle system. Each particle system was fluorescently labeled through the attachment of *N*-hydroxysuccinimide (NHS)-activated Alexa Fluor (AF) 488 (AF488-NHS) and incubated with human whole blood and human "washed" blood. The latter condition required separation of whole blood into plasma and blood cells via repeated centrifugation and washing steps in phosphate-buffered saline (PBS). In the absence of plasma, the nanoparticles incubated in washed blood may not form a biomolecular corona, thus allowing elucidation of the influence of the corona on phagocytosis.

Cell association was determined for both incubation conditions by flow cytometry after incubation of the particles at 37 °C for 1 h, following phenotyping of the individual immune cells. A recently published gating strategy allows identification of individual cell types (Figure S7).[50] For both incubation media, human whole blood and human washed blood, all particle systems showed a relatively low association with phagocytic cells (neutrophils, monocytes, dendritic cells) and negligible association with non-phagocytic cells (T cells, B cells, NK cells)(Figure 8A). The highest level of cell–particle association in human whole blood was detected for monocytes, with approximately 26% (OG), 44% (OG-PNIPAM 1), and 37% (OG-PNIPAM 2) of cells positive for OG and the OG-PNIPAM-conjugated nanoparticles. Generally, no statistically significant differences were observed between the individual particle systems. In contrast, in human washed blood, OG had the lowest number % association, which increased for the OG-PNIPAM-conjugated

nanoparticles, with OG-PNIPAM 2 displaying the highest number % association with monocytes. We hypothesize that biologically relevant surface characteristics of the particles are shielded upon formation of a biomolecular corona. Thus, biological differences between particle types become apparent only in washed blood. Furthermore, the association of OG-PNIPAM 2 with monocytes increased from 37% to 61% upon incubation in human washed blood (Figure 8B). These data indicate that the absence of plasma proteins in the incubation environment enhances cell–nanoparticle interactions, likely from the PNIPAM creating hydrophobic patches at 37 °C, resulting in a slight increase in cell association. The increase in association with dendritic cells after incubation in human washed blood did not reach statistical significance because of the low number of dendritic cells detected (Table S3).

For analysis of how the PNIPAM functionalization affects inflammatory responses, the particles were mixed with low-heparinized human whole blood and incubated for 1 h at 37 °C in a dynamic Chandler loop system.[16] CD11b expression on neutrophils was measured to determine cellular inflammatory response (Figure 8C), and the complement fragment C5a was measured as a marker of plasmatic activation (Figure 8D).

The presence of OG-based particles in general resulted in neutrophil activation and further supported the propagation of the complement cascade to C5 activation and formation of C5a. Unmodified OG particles and OG-PNIPAM 2 had similar effects on the CD11b expression of neutrophils (Figure 8C), whereby the plasmatic response was strongest for OG-PNIPAM 2 particles (Figure 8D). For both inflammation responses, OG-PNIPAM 1 particles showed the lowest activation.

Overall, the functionalization of OG with temperature responsive PNIPAM, from the protein component within glycogen, does not significantly change the association of the particles with

human immune cells. The cellular inflammation response was found to be similar between the OG and OG-PNIPAM 2 particle systems, however reduced for the OG-PNIPAM 1 particle system. The humoral inflammation response, on the other hand, was found to be similar for the OG and OG-PNIPAM 1 particle system, whereas increased for the OG-PNIPAM 2 particle system. The reason for these differences is not clear, but possibility due to a complex interplay of differing surface chemistry, molecular weight, and particle size. As the incubation experiments were performed at 37 °C, it is expected that the OG-PNIPAM nanoparticle systems have a different particle size distribution than OG. Functionalization with PNIPAM was instrumental for examining both the effect of hydrophobicity and size on glycogen association with immune cells; the findings show that the low-association property that is inherent for OG is retained. It is anticipated that other functional monomers can also be photopolymerized from the protein component of glycogen in a similar manner.

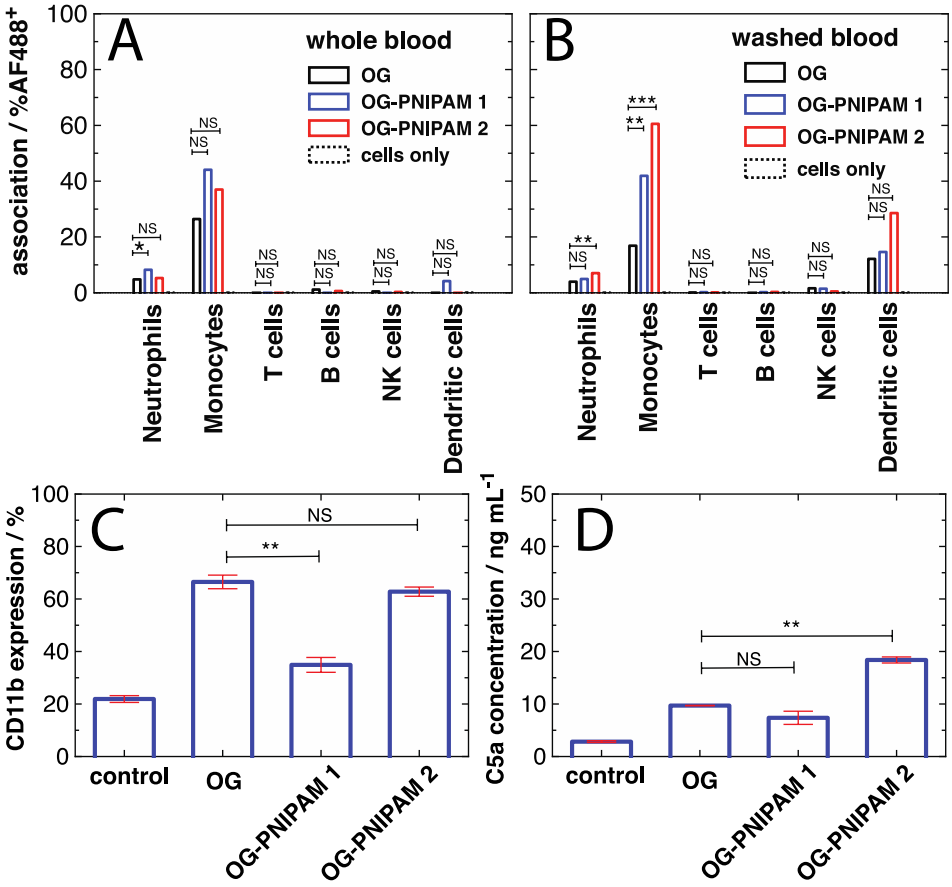

Figure 8. Association of Alexa-Fluor 488-labeled particles with immune cells in (A) whole and (B) washed blood at 37 °C. (C) CD11b expression of neutrophils as a marker of cellular inflammation activation (normalized to 100 units mL^{-1} lipopolysaccharide (LPS)) and (D) plasma complement C5a concentration as a marker of humoral inflammation, both in comparison to a blank control sample of blood without particles present. Error bars represent standard deviations ($n = 3$). Statistical significance was determined by a two-tailed *t*-test and is reported as $*p < 0.05$, $**p < 0.01$, and $***p < 0.001$, NS is non-significant.

To improve reproducibility, reporting, and re-analysis, this study conforms to the MIRIBEL standard,[52] and a companion checklist is provided in the Supporting Information.

CONCLUSIONS

Glycogen nanoparticles contain a small, but structurally significant amount of protein. Among the common commercial sources of glycogen examined, OG featured the largest amount of protein. When these proteins were degraded enzymatically ex situ with protease, the average particle size decreased and most particles became more spherical, as determined from pair distribution functions from SAXS analysis. This result likely reflects the presence of proteins towards the particles' surface. These particle-bound proteins were examined as anchor points for the thiol-initiated photopolymerization of NIPAM from the OG nanoparticles. Different aqueous volume fractions were studied, which resulted in control over the extent of polymerization on the particles. Following polymerization, there was a reduction in the quantity of free thiols on the particles, with a corresponding increase in the molecular weight of the nanoparticles. The resulting OG-PNIPAM particles showed switchable temperature-dependent aggregation properties as the LCST of PNIPAM (32 °C) was approached, where the aggregation was reversible and controllable. This offers a surface property that can be exploited for controlled aggregation at biologically relevant temperatures (37 °C).

The ability of these surface chains to influence human immune cell recognition and inflammation responses was analyzed by performing human blood incubation assays. Endowing a temperature-functionality to the OG nanoparticles did not significantly influence the association of the particles with human immune cells, demonstrating that the low-association behavior of OG was preserved post-modification. The modified particles caused similar activation of neutrophils and the complement system in comparison to OG, with some differences between particle types that may be related to differing surface properties. The PNIPAM component could be removed enzymatically by protease enzymes, where the glycogen retained its original biodegradability. The present findings highlight a simple strategy to functionalize glycogen nanoparticles with

temperature responsiveness while maintaining low nonspecific cell association and particle biodegradability.

ASSOCIATED CONTENT

Supporting Information. Experimental details for the SEC-SAXS, GPC, particle sizes with temperature, ^{1}H NMR spectra of protease digested samples, and the human blood assay studies, along with the MIRIBEL checklist for reporting research in bio-nano science.

AUTHOR INFORMATION

Corresponding Author

*E-mail: besford@ipfdd.de

*E-mail: fcaruso@unimelb.edu.au

*E-mail: francesca.cavalieri@rmit.edu.au

ORCID

Quinn A. Besford: 0000-0002-1779-9176

Alessia C. G. Weiss: 0000-0001-7274-551X

Timothy M. Ryan: 0000-0001-7274-551X

Pietro Pachin Tomanin: 0000-0002-5547-3863

Carsten Werner: 0000-0003-0189-3448

Andreas Fery: 0000-0001-6692-3762

Frank Caruso: 0000-0002-0197-497X

Francesca Cavalieri: 0000-0001-5391-5069

Notes

The authors declare no competing financial interest.

ACKNOWLEDGMENT

Part of this work was performed at the Australian Synchrotron (Q.A.B., AS173/SAXS/12732). This research was conducted and funded in part by the Alexander von Humboldt foundation (Q.A.B.) and the Australian Research Council (ARC) Centre of Excellence in Convergent Bio-Nano Science and Technology (project number CE140100036). F.C. acknowledges the award of a National Health and Medical Research Council Senior Principal Research Fellowship (GNT1135806). We gratefully acknowledge Dr. Nigel Kirby and Dr. Andrew Christofferson for support with the synchrotron experiments, Christina Harnisch for assistance with the GPC experiments, and Dr. Tian Zheng and Dr. Matthew Biviano for assistance with the AFM measurements. This work was performed in part at the Materials Characterization and Fabrication Platform (MCFP) of The University of Melbourne.

REFERENCES

(1) Taraballi, F.; Sushnitha, M.; Tsao, C.; Bauza, G.; Liverani, C.; Shi, A.; Tasciotti, E. Biomimetic Tissue Engineering: Tuning the Immune and Inflammatory Response to Implantable Biomaterials. *Adv. Healthc. Mater.* **2018,** *7*, e1800490.

(2) Rattan, R.; Bhattacharjee, S.; Zong, H.; Swain, C.; Siddiqui, M. A.; Visovatti, S. H.; Kanthi, Y.; Desai, S.; Pinsky, D. J.; Goonewardena, S. N. Nanoparticle-macrophage Interactions: A

Balance Between Clearance and Cell-specific Targeting. *Bioorg. Med. Chem.* **2017,** *25*, 4487-4496.

(3) Wang, J.; Liu, G. Imaging Nano-Bio Interactions in the Kidney: Toward a Better Understanding of Nanoparticle Clearance. *Angew. Chem. Int. Ed. Engl.* **2018,** *57*, 3008-3010.

(4) Cassano, D.; Mapanao, A.-K.; Summa, M.; Vlamidis, Y.; Giannone, G.; Santi, M.; Guzzolino, E.; Pitto, L.; Poliseno, L.; Bertorelli, R.; Voliani, V. Biosafety and Biokinetics of Noble Metals: The Impact of Their Chemical Nature. *ACS Appl. Bio. Mater.* **2019,** *2*, 4464-4470.

(5) Zhao, H.; Li, L.; Zhan, H.; Chu, Y.; Sun, B. Mechanistic Understanding of the Engineered Nanomaterial-Induced Toxicity on Kidney. *J. Nanomater.* **2019,** *2019*, 1-12.

(6) Saha, K.; Rahimi, M.; Yazdani, M.; Kim, S. T.; Moyano, D. F.; Hou, S.; Das, R.; Mout, R.; Rezaee, F.; Mahmoudi, M.; Rotello, V. M. Regulation of Macrophage Recognition through the Interplay of Nanoparticle Surface Functionality and Protein Corona. *ACS Nano* **2016,** *10*, 4421-4430.

(7) Calatayud, M. P.; Sanz, B.; Raffa, V.; Riggio, C.; Ibarra, M. R.; Goya, G. F. The Effect of Surface Charge of Functionalized Fe3O4 Nanoparticles on Protein Adsorption and Cell Uptake. *Biomaterials* **2014,** *35*, 6389-6399.

(8) Garcia-Alvarez, R.; Hadjidemetriou, M.; Sanchez-Iglesias, A.; Liz-Marzan, L. M.; Kostarelos, K. In Vivo Formation of Protein Corona on Gold Nanoparticles: The Effect of their Size and Shape. *Nanoscale* **2018,** *10*, 1256-1264.

(9) Obst, K.; Yealland, G.; Balzus, B.; Miceli, E.; Dimde, M.; Weise, C.; Eravci, M.; Bodmeier, R.; Haag, R.; Calderon, M.; Charbaji, N.; Hedtrich, S. Protein Corona Formation on Colloidal Polymeric Nanoparticles and Polymeric Nanogels: Impact on Cellular Uptake, Toxicity, Immunogenicity, and Drug Release Properties. *Biomacromolecules* **2017,** *18*, 1762-1771.

(10) Zou, H.; Wang, Z.; Feng, M. Nanocarriers with Tunable Surface Properties to Unblock Bottlenecks in Systemic Drug and Gene Delivery. *J. Control. Release* **2015,** *214*, 121-133.

(11) Miceli, E.; Kar, M.; Calderón, M. Interactions of Organic Nanoparticles with Proteins in Physiological Conditions. *J. Mater. Chem. B* **2017,** *5*, 4393-4405.

(12) Van de Walle, A.; Plan Sangnier, A.; Abou-Hassan, A.; Curcio, A.; Hemadi, M.; Menguy, N.; Lalatonne, Y.; Luciani, N.; Wilhelm, C. Biosynthesis of Magnetic Nanoparticles from Nano-degradation Products Revealed in Human Stem Cells. *Proc. Natl. Acad. Sci. U. S. A.* **2019,** *116*, 4044-4053.

(13) Balfourier, A.; Luciani, N.; Wang, G.; Lelong, G.; Ersen, O.; Khelfa, A.; Alloyeau, D.; Gazeau, F.; Carn, F. Unexpected Intracellular Biodegradation and Recrystallization of Gold Nanoparticles. *Proc. Natl. Acad. Sci. U. S. A.* **2020,** *117*, 103-113.

(14) Boitard, C.; Curcio, A.; Rollet, A. L.; Wilhelm, C.; Menager, C.; Griffete, N. Biological Fate of Magnetic Protein-Specific Molecularly Imprinted Polymers: Toxicity and Degradation. *ACS Appl. Mater. Interfaces* **2019,** *11*, 35556-35565.

(15) Crivelli, B.; Perteghella, S.; Bari, E.; Sorrenti, M.; Tripodo, G.; Chlapanidas, T.; Torre, M. L. Silk Nanoparticles: From Inert Supports to Bioactive Natural Carriers for Drug Delivery. *Soft Matter* **2018,** *14*, 546-557.

(16) Maitz, M. F.; Sperling, C.; Wongpinyochit, T.; Herklotz, M.; Werner, C.; Seib, F. P. Biocompatibility Assessment of Silk Nanoparticles: Hemocompatibility and Internalization by Human Blood Cells. *Nanomedicine* **2017,** *13*, 2633-2642.

(17) Faivre, D.; Schuler, D. Magnetotactic Bacteria and Magnetosomes. *Chem. Rev.* **2008,** *108*, 4875-4898.

(18) He, J.; Fan, K.; Yan, X. Ferritin Drug Carrier (FDC) for Tumor Targeting Therapy. *J. Control. Release* **2019,** *311-312*, 288-300.

(19) Prats, C.; Graham, T. E.; Shearer, J. The Dynamic Life of the Glycogen Granule. *J. Biol. Chem.* **2018,** *293*, 7089-7098.

(20) Ng, K. K.; Lovell, J. F.; Zheng, G. Lipoprotein-inspired Nanoparticles for Cancer Theranostics. *Acc. Chem. Res.* **2011,** *44*, 1105-1113.

(21) Park, J. S.; Cho, M. K.; Lee, E. J.; Ahn, K. Y.; Lee, K. E.; Jung, J. H.; Cho, Y.; Han, S. S.; Kim, Y. K.; Lee, J. A Highly Sensitive and Selective Diagnostic Assay Based on Virus Nanoparticles. *Nat. Nanotechnol.* **2009,** *4*, 259-264.

(22) Stanley, S. Biological Nanoparticles and their Influence on Organisms. *Curr. Opin. Biotechnol.* **2014,** *28*, 69-74.

(23) Pattanashetti, N. A.; Heggannavar, G. B.; Kariduraganavar, M. Y. Smart Biopolymers and their Biomedical Applications. *Procedia Manuf.* **2017,** *12*, 263-279.

(24) Besford, Q. A.; Cavalieri, F.; Caruso, F. Glycogen as a Building Block for Advanced Biological Materials. *Adv. Mater.* **2019**, e1904625.

(25) Gopinath, V.; Saravanan, S.; Al-Maleki, A. R.; Ramesh, M.; Vadivelu, J. A Review of Natural Polysaccharides for Drug Delivery Applications: Special Focus on Cellulose, Starch and Glycogen. *Biomed. Pharmacother.* **2018,** *107*, 96-108.

(26) Besford, Q. A.; Wojnilowicz, M.; Suma, T.; Bertleff-Zieschang, N.; Caruso, F.; Cavalieri, F. Lactosylated Glycogen Nanoparticles for Targeting Prostate Cancer Cells. *ACS Appl. Mater. Interfaces* **2017,** *9*, 16869-16879.

(27) Wojnilowicz, M.; Besford, Q. A.; Wu, Y. L.; Loh, X. J.; Braunger, J. A.; Glab, A.; Cortez-Jugo, C.; Caruso, F.; Cavalieri, F. Glycogen-nucleic Acid Constructs for Gene Silencing in Multicellular Tumor Spheroids. *Biomaterials* **2018,** *176*, 34-49.

(28) Filippov, S. K.; Sedlacek, O.; Bogomolova, A.; Vetrik, M.; Jirak, D.; Kovar, J.; Kucka, J.; Bals, S.; Turner, S.; Stepanek, P.; Hruby, M. Glycogen as a Biodegradable Construction Nanomaterial for In Vivo use. *Macromol. Biosci.* **2012,** *12*, 1731-1738.

(29) Lu, F.; Mosley, Y. C.; Rodriguez Rosales, R. J.; Carmichael, B. E.; Elesela, S.; Yao, Y.; HogenEsch, H. Alpha-D-glucan Nanoparticulate Adjuvant Induces a Transient Inflammatory Response at the Injection Site and Targets Antigen to Migratory Dendritic Cells. *NPJ Vaccines* **2017,** *2*, 4.

(30) Zhang, X.; Zhou, J.; Ying, H.; Zhou, Y.; Lai, J.; Chen, J. Glycogen as a Cross-Linking Agent of Collagen and Nanohydroxyapatite To Form Hydrogels for bMSC Differentiation. *ACS Sustain. Chem. Eng.* **2020,** *8*, 2106-2114.

(31) Pacchin Tomanin, P.; Zhou, J.; Amodio, A.; Cimino, R.; Glab, A.; Cavalieri, F.; Caruso, F. Nanoengineering Multifunctional Hybrid Interfaces using Adhesive Glycogen Nanoparticles. *J. Mater. Chem. B* **2020**, *8*, 4851-4858.

(32) Rabyk, M.; Hruby, M.; Vetrik, M.; Kucka, J.; Proks, V.; Parizek, M.; Konefal, R.; Krist, P.; Chvatil, D.; Bacakova, L.; Slouf, M.; Stepanek, P. Modified Glycogen as Construction Material for Functional Biomimetic Microfibers. *Carbohydr. Polym.* **2016,** *152*, 271-279.

(33) Vetrik, M.; Pradny, M.; Kobera, L.; Slouf, M.; Rabyk, M.; Pospisilova, A.; Stepanek, P.; Hruby, M. Biopolymer-based Degradable Nanofibres from Renewable Resources Produced by Freeze-drying. *RSC Advances* **2013,** *3*, 15282-15289.

(34) Hu, Z.; Deng, B.; Tan, X.; Gan, H.; Li, C.; Nada, S. S.; Sullivan, M. A.; Li, J.; Jiang, X.; Li, E.; Gilbert, R. G. Diurnal Changes of Glycogen Molecular Structure in Healthy and Diabetic Mice. *Carbohydr. Polym.* **2018,** *185*, 145-152.

(35) Sullivan, M. A.; Aroney, S. T.; Li, S.; Warren, F. J.; Joo, J. S.; Mak, K. S.; Stapleton, D. I.; Bell-Anderson, K. S.; Gilbert, R. G. Changes in Glycogen Structure over Feeding Cycle Sheds New Light on Blood-glucose Control. *Biomacromolecules* **2014,** *15*, 660-665.

(36) Ryu, J. H.; Drain, J.; Kim, J. H.; McGee, S.; Gray-Weale, A.; Waddington, L.; Parker, G. J.; Hargreaves, M.; Yoo, S. H.; Stapleton, D. Comparative Structural Analyses of Purified Glycogen Particles from Rat Liver, Human Skeletal Muscle and Commercial Preparations. *Int. J. Biol. Macromol.* **2009,** *45*, 478-482.

(37) Besford, Q. A.; Sullivan, M. A.; Zheng, L.; Gilbert, R. G.; Stapleton, D.; Gray-Weale, A. The Structure of Cardiac Glycogen in Healthy Mice. *Int. J. Biol. Macromol.* **2012,** *51*, 887-891.

(38) Besford, Q. A.; Zeng, X. Y.; Ye, J. M.; Gray-Weale, A. Liver Glycogen in Type 2 Diabetic Mice is Randomly Branched as Enlarged Aggregates with Blunted Glucose Release. *Glycocon. J.* **2016,** *33*, 41-51.

(39) Tan, X.; Sullivan, M. A.; Nada, S. S.; Deng, B.; Schulz, B. L.; Gilbert, R. G. Proteomic Investigation of the Binding Agent between Liver Glycogen beta Particles. *ACS Omega* **2018,** *3*, 3640-3645.

(40) Lu, F.; Mencia, A.; Bi, L.; Taylor, A.; Yao, Y.; HogenEsch, H. Dendrimer-like Alpha-d-glucan Nanoparticles Activate Dendritic Cells and are Effective Vaccine Adjuvants. *J. Control. Release* **2015,** *204*, 51-59.

(41) Kakutani, R.; Adachi, Y.; Kajiura, H.; Takata, H.; Kuriki, T.; Ohno, N. Relationship Between Structure and Immunostimulating Activity of Enzymatically Synthesized Glycogen. *Carbohydr. Res.* **2007,** *342*, 2371-2379.

(42) Masuko, T.; Minami, A.; Iwasaki, N.; Majima, T.; Nishimura, S.; Lee, Y. C. Carbohydrate Snalysis by a Phenol-sulfuric Acid Method in Microplate Format. *Anal. Biochem.* **2005,** *339*, 69-72.

(43) Ryan, T. M.; Trewhella, J.; Murphy, J. M.; Keown, J. R.; Casey, L.; Pearce, F. G.; Goldstone, D. C.; Chen, K.; Luo, Z.; Kobe, B.; McDevitt, C. A.; Watkin, S. A.; Hawley, A. M.; Mudie, S. T.; Samardzic Boban, V.; Kirby, N. An Optimized SEC-SAXS System Enabling High X-ray Dose for Rapid SAXS Assessment with Correlated UV Measurements for Biomolecular Structure Analysis. *J. Appl. Crystallogr.* **2018,** *51*, 97-111.

(44) Kirby, N. M.; Mudie, S. T.; Hawley, A. M.; Cookson, D. J.; Mertens, H. D. T.; Cowieson, N.; Samardzic-Boban, V. A Low-background-intensity Focusing Small-angle X-ray Scattering Undulator Beamline. *J. Appl. Crystallogr.* **2013,** *46*, 1670-1680.

(45) Kirby, N.; Cowieson, N.; Hawley, A. M.; Mudie, S. T.; McGillivray, D. J.; Kusel, M.; Samardzic-Boban, V.; Ryan, T. M. Improved Radiation Dose Efficiency in Solution SAXS using a Sheath Flow Sample Environment. *Acta Crystallogr. D Struct. Biol.* **2016,** *72*, 1254-1266.

(46) Rai, N.; Nollmann, M.; Spotorno, B.; Tassara, G.; Byron, O.; Rocco, M. SOMO (SOlution MOdeler) Differences between X-Ray- and NMR-derived Bead Models Suggest a Role for Side Chain Flexibility in Protein Hydrodynamics. *Structure* **2005,** *13*, 723-734.

(47) Svergun, D. I. Determination of the Regularization Parameter in Indirect-Transform Methods Using Perceptual Criteria. *J. Appl. Cryst.* **1992,** *25*, 495-503.

(48) Franke, D.; Svergun, D. I. DAMMIF: A Program for Rapid Ab-initio Shape Determination in Small-angle Scattering. *J. Appl. Cryst.* **2009,** *42*, 342-346.

(49) Franke, D.; Petoukhov, M. V.; Konarev, P. V.; Panjkovich, A.; Tuukkanen, A.; Mertens, H. D. T.; Kikhney, A. G.; Hajizadeh, N. R.; Franklin, J. M.; Jeffries, C. M.; Svergun, D. I. ATSAS 2.8: A Comprehensive Data Analysis Suite for Small-angle Scattering from Macromolecular Solutions. *J .Appl. Crystallogr.* **2017,** *50*, 1212-1225.

(50) Weiss, A. C. G.; Kelly, H. G.; Faria, M.; Besford, Q. A.; Wheatley, A. K.; Ang, C. S.; Crampin, E. J.; Caruso, F.; Kent, S. J. Link between Low-Fouling and Stealth: A Whole Blood Biomolecular Corona and Cellular Association Analysis on Nanoengineered Particles. *ACS Nano* **2019,** *13*, 4980-4991.

(51) Gardner, R. A. An Examination of the Fluid Mechanics and Thrombus Formation Time Parameters in a Chandler Rotating Loop System. *J. Lab. Clin. Med.* **1974,** *84*, 494-508.

(52) Faria, M.; Bjornmalm, M.; Thurecht, K. J.; Kent, S. J.; Parton, R. G.; Kavallaris, M.; Johnston, A. P. R.; Gooding, J. J.; Corrie, S. R.; Boyd, B. J.; Thordarson, P.; Whittaker, A. K.; Stevens, M. M.; Prestidge, C. A.; Porter, C. J. H.; Parak, W. J.; Davis, T. P.; Crampin, E. J.; Caruso, F. Minimum Information Reporting in Bio-nano Experimental Literature. *Nat. Nanotechnol.* **2018,** *13*, 777-785.

(53) Stapleton, D.; Nelson, C.; Parsawar, K.; McClain, D.; Gilbert-Wilson, R.; Barker, E.; Rudd, B.; Brown, K.; Hendrix, W.; O'Donnell, P.; Parker, G. Analysis of Hepatic Glycogen-associated Proteins. *Proteomics* **2010,** *10*, 2320-2329.

(54) Roach, P. J.; Depaoli-Roach, A. A.; Hurley, T. D.; Tagliabracci, V. S. Glycogen and its Metabolism: Some New Developments and Old Themes. *Biochem. J.* **2012,** *441*, 763-787.

(55) Manners, D. J. Recent Developments in Our Understanding of Glycogen Structure. *Carbohydr. Polym.* **1991,** *16*, 37-82.

(56) Visuttijai, K.; Hedberg-Oldfors, C.; Thomsen, C.; Glamuzina, E.; Kornblum, C.; Tasca, G.; Hernandez-Lain, A.; Sandstedt, J.; Dellgren, G.; Roach, P.; Oldfors, A. Glycogenin is Dispensable for Glycogen Synthesis in Human Muscle, and Glycogenin Deficiency Causes Polyglucosan Storage. *J. Clin. Endocrinol. Metab.* **2020,** *105*, 557-566.

(57) Testoni, G.; Duran, J.; Garcia-Rocha, M.; Vilaplana, F.; Serrano, A. L.; Sebastian, D.; Lopez-Soldado, I.; Sullivan, M. A.; Slebe, F.; Vilaseca, M.; Munoz-Canoves, P.; Guinovart, J. J. Lack of Glycogenin Causes Glycogen Accumulation and Muscle Function Impairment. *Cell Metab.* **2017,** *26*, 256-266.

(58) Tan, X.; Sullivan, M. A.; Gao, F.; Li, S.; Schulz, B. L.; Gilbert, R. G. A New Non-degradative Method to Purify Glycogen. *Carbohydr. Polym.* **2016,** *147*, 165-170.

(59) Goldhahn, C.; Schubert, J.; Schlaad, H.; Ferri, J. K.; Fery, A.; Chanana, M. Synthesis of Metal@Protein@Polymer Nanoparticles with Distinct Interfacial and Phase Transfer Behavior. *Chem. Mater.* **2018,** *30*, 6717-6727.

(60) Sullivan, M. A.; O'Connor, M. J.; Umana, F.; Roura, E.; Jack, K.; Stapleton, D. I.; Gilbert, R. G. Molecular Insights into Glycogen Alpha-particle Formation. *Biomacromolecules* **2012,** *13*, 3805-3813.

(61) Bertoldo, M.; Zampano, G.; Suffner, L.; Liberati, E.; Ciardelli, F. Oxidation of glycogen "molecular nanoparticles" by periodate. *Polym. Chem.* **2013,** *4*, 653-661.

(62) Khine, Y. Y.; Ganda, S.; Stenzel, M. H. Covalent Tethering of Temperature Responsive pNIPAm onto TEMPO-Oxidized Cellulose Nanofibrils via Three-Component Passerini Reaction. *ACS Macro Letters* **2018,** *7*, 412-418.

(63) Schmidt, S.; Zeiser, M.; Hellweg, T.; Duschl, C.; Fery, A.; Möhwald, H. Adhesion and Mechanical Properties of PNIPAM Microgel Films and Their Potential Use as Switchable Cell Culture Substrates. *Adv. Funct. Mater.* **2010,** *20*, 3235-3243.

(64) Nickels, J. D.; Atkinson, J.; Papp-Szabo, E.; Stanley, C.; Diallo, S. O.; Perticaroli, S.; Baylis, B.; Mahon, P.; Ehlers, G.; Katsaras, J.; Dutcher, J. R. Structure and Hydration of Highly-Branched, Monodisperse Phytoglycogen Nanoparticles. *Biomacromolecules* **2016,** *17*, 735-743.

(65) Saei, A. A.; Yazdani, M.; Lohse, S. E.; Bakhtiary, Z.; Serpooshan, V.; Ghavami, M.; Asadian, M.; Mashaghi, S.; Dreaden, E. C.; Mashaghi, A.; Mahmoudi, M. Nanoparticle Surface Functionality Dictates Cellular and Systemic Toxicity. *Chem. Mater.* **2017,** *29*, 6578-6595.

(66) Liu, Y.; Yin, Y.; Wang, L.; Zhang, W.; Chen, X.; Yang, X.; Xu, J.; Ma, G. Surface Hydrophobicity of Microparticles Modulates Adjuvanticity. *J. Mater. Chem. B* **2013,** *1*, 3888-3896.

For Table of Contents use only